

Article

Wind-Induced Aerodynamic Effects on Set-Back Tall Buildings Using LES

Nan-Ting Yu ^{1,2,3}, Wei-Hao Li ¹, Yu Zheng ¹ and Wei-Bin Yuan ^{1,3,*}

¹ College of Civil Engineering, Zhejiang University of Technology, Hangzhou 310023, China; nantingyu@zjut.edu.cn (N.-T.Y.); 2112106027@zjut.edu.cn (W.-H.L.); 211122060024@zjut.edu.cn (Y.Z.)

² Huzhou Green New Material Co., Ltd., Huzhou 313023, China

³ Zhejiang Key Laboratory of Civil Engineering Structures and Disaster Prevention and Mitigation Technology, Hangzhou 310023, China

* Correspondence: yuanwb@zjut.edu.cn

Abstract: Set-back modification represents a dependable method to reducing the wind effects on high-rise buildings, but the flow mechanism and aerodynamic responses of set-back tall buildings have not been explored systematically. Using the square building as the benchmark model, six set-back building models with varying steps and sizes were chosen for numerical simulation in this study. The results of mean wind pressure and local wind force distribution, power spectral densities of base moment, flow field, and structural response of the proposed building models are compared and analysed using the Large Eddy Simulation (LES) technique. The results demonstrate that the aerodynamic performance of set-back tall buildings dramatically improved, with the actual optimization in the cross-wind direction being more significant. Generally, a single set-back measure can enhance the aerodynamic performance of high-rise buildings more effectively than a double set-back measure. The outcome of this study provides an aerodynamic design guide for set-back tall buildings.

Keywords: high-rise buildings; set-back shape; LES; wind force; wind response



Citation: Yu, N.-T.; Li, W.-H.; Zheng, Y.; Yuan, W.-B. Wind-Induced Aerodynamic Effects on Set-Back Tall Buildings Using LES. *Buildings* **2024**, *14*, 1252. <https://doi.org/10.3390/buildings14051252>

Academic Editor: Shaohong Cheng

Received: 1 April 2024

Revised: 24 April 2024

Accepted: 26 April 2024

Published: 29 April 2024



Copyright: © 2024 by the authors. Licensee MDPI, Basel, Switzerland. This article is an open access article distributed under the terms and conditions of the Creative Commons Attribution (CC BY) license (<https://creativecommons.org/licenses/by/4.0/>).

1. Introduction

High-rise buildings are particularly susceptible to wind due to their slender shapes and low damping ratios. Hence, estimating and mitigating wind effects are crucial for wind and structural engineers [1]. The main wind resistance measures for high-rise buildings include structural control, mechanical vibration control, and aerodynamic optimization. Among them, aerodynamic optimization offers improved economic performance, enhanced security, and greater efficiency [2,3]. It reduces the wind loads on the buildings by altering the wind field around the structure [4].

There are two approaches: corner (minor) modification and outer shape (major) modification for aerodynamic optimization. Major modification of buildings not only facilitates access to natural light and enhances aesthetics but also provides more flexible usage space [5]. Currently, major modification is the primary strategy for mitigating wind force effects on high-rise buildings [6,7], such as tapered, helical, inclined, opening, and set-back buildings (see Figure 1). Cooper et al. [8] have studied the wind effects on tapered buildings through wind tunnel tests, and their results show that tapered measures could diminish cross-wind aerodynamic forces. Kim et al. [9] have conducted wind tunnel experiments using a rocking vibration model to investigate the aerodynamic damping of a 180° twisted super-tall building. It was shown that the helical model exhibited superior aerodynamic behaviour compared to the square model. Chen et al. [10] have evaluated the aerodynamic characteristics of an inclined square prism through wind tunnel tests and Large Eddy Simulation (LES). The results showed that the inclination could suppress the vortex shedding of the building. Wind loads and wind speed amplification on high-rise

buildings with openings were investigated by Chen et al. [11]. The results show that the opening could lessen the wind load in the along-wind direction.

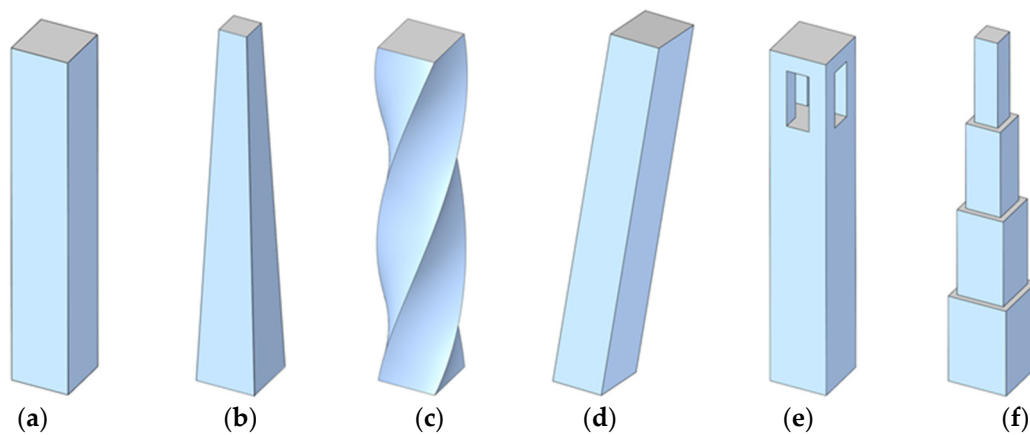


Figure 1. Example of major modifications: (a) basic shape; (b) tapered shape; (c) helical shape; (d) inclined shape; (e) opening shape; (f) set-back shape.

To a certain extent, set-back buildings exhibit superior aerodynamic performance compared to the other major modifications mentioned above [12]. For example, Kim et al. [13] have carried out wind tunnel tests on 13 super-tall buildings with various atypical building shapes to assess wind load effects, and it was demonstrated that set-back buildings had the lowest peak normal stresses. Tanaka et al. [14] have conducted a series of wind tunnel experiments to determine the aerodynamic forces and wind pressures on high-rise buildings with corner cut, set-back, or helical configurations, and they found that set-back buildings could enhance aerodynamic performance in the along-wind and cross-wind directions compared to other major modifications. The spatio-temporal characteristics of pressure fluctuations on tapered and set-back buildings were investigated by Kim and Kanda [15], and it was found that the fluctuating lift force on set-back buildings was significantly lower than that on tapered buildings.

Compared to wind tunnel tests, numerical simulation can capture the details of a flow field around building models. Bairagi and Dalui [16,17] have investigated the wind pressure distribution and wind speed characteristics of set-back buildings by using Reynolds-averaged Navier–Stokes simulation (RANS), and they obtained the time average wind load and flow. Rajasekarababu et al. [18] have studied the flow field distribution of set-back tall buildings using Unsteady Reynolds-averaged Navier–Stokes simulation (URANS), and the results indicated that URANS was capable of simulating the distribution of mean and fluctuating wind pressure, but was unable to explicitly capture the distribution of flow field in the downstream re-circulation. Subsequently, both Delayed Detached Eddy Simulation (DDES) and Improved Delayed Detached Eddy Simulation (IDDES) were used to evaluate the flow structure around set-back buildings by Rajasekarababu et al. [19], and they found that IDDES could more accurately predict the downstream re-circulation of set-back buildings than DDES. However, the aforementioned numerical simulations are unable to capture the details of transient flow around the surface of set-back buildings.

It is known that LES can simulate near-wall flow and complex flow structures, thereby enhancing the improvement in the resolution of a calculated flow field. Previous research has confirmed the validity and accuracy of LES through comparisons with wind tunnel tests and other numerical simulation methods [20–22]. The wind load and aerodynamic performance of the square and trapped building models were estimated by using LES [23,24]. However, limited research has been conducted on the wind effect on set-back tall buildings using the LES technique.

This paper presents a numerical investigation on the flow mechanism and aerodynamic performance of set-back tall buildings by using LES. The results of mean wind

pressure and local wind force distribution, power spectral densities of base moment, instantaneous vortex structure, time-averaged flow field, and structural response of different set-back measures are discussed comprehensively. The findings provide an aerodynamic design guide for set-back tall buildings.

2. Methodology

2.1. Geometry and Measurement Taps

To facilitate comparison with the results from the existing wind tunnel test, the scale ratio of the numerical model was set to 1:500. Seven high-rise building models, categorized into two groups with an identical ratio of depth (D), width (W), and height (H) 1:1:6, were studied. The benchmark model is a rectangular block with $D = 100$ mm, $W = 100$ mm, and $H = 600$ mm (see Figure 2a). The first group (Group 1) comprised three single set-backs (case 2, case 3, and case 4); the height of the set-back was $H/2$, and the edges of set-back were distanced at $0.1D$, $0.15D$, and $0.2D$ far from the edge of base, respectively (see Figure 2b). Similarly, the second group (Group 2) encompassed three double set-backs (case 5, case 6, and case 7). The heights of the two set-backs were $H/3$, with the edges of the first set-back at $0.05D$, $0.075D$, and $0.1D$ far from the edge of base, and the edges of the second set-back were at $0.05D$, $0.075D$, and $0.1D$ far from the edge of the first set-back, respectively (see Figure 2c).

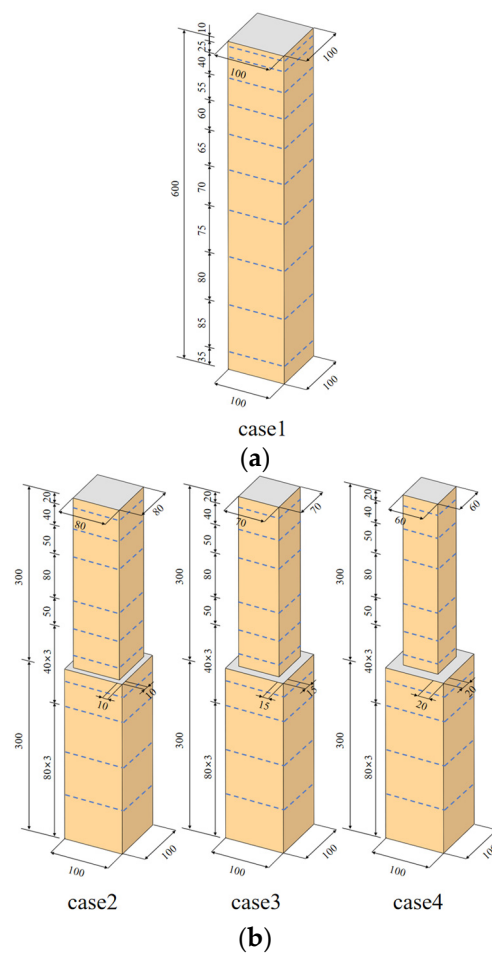


Figure 2. Cont.

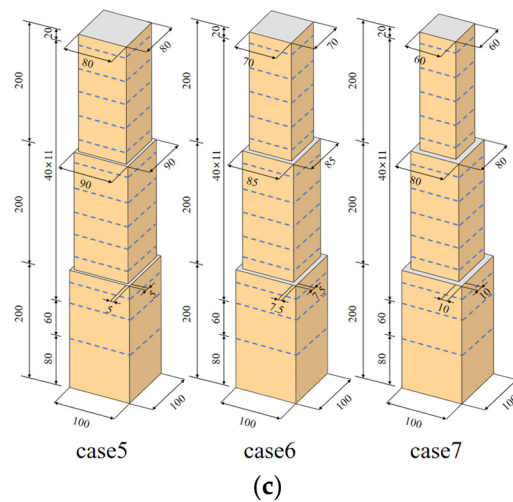


Figure 2. Different set-back building models: (a) benchmark; (b) single set-back; (c) double set-back.

To capture the details of the wind fields surrounding the set-backs accurately, measurement taps were encrypted on the surface of set-backs. As shown in Figure 2, for the benchmark model and the first group, the measurement taps were arranged in 10 layers, while for the second group, the measurement layers were organized into 13 layers.

2.2. Domain and Meshing

The dimensions of the computational domain were set as $6H \times 15H \times 3H$, and the origin coordinate was positioned at the bottom centre of the model, as shown in Figure 3. The distance between the inlet and the model centre was $5H$, and the distance between the outlet and the model centre was $10H$. In addition, the model centre was $3H$ away from both the lateral and top sides. In the numerical simulation, the blockage rate was set to not exceed 5%, which is in accordance with the requirement of specification [25].

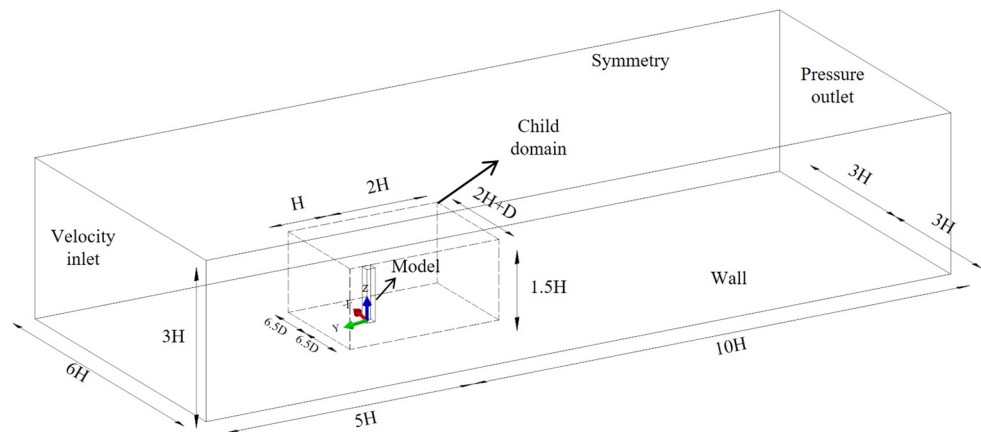


Figure 3. The computational domain with boundary conditions.

The computational grid was fully structured. A child domain with a stretching ratio of 1.05 was constructed around the model to enhance the accuracy and trace small eddies [26]. The dimensions of the refined mesh region were $(2H + D) \times 3H \times 1.5H$, and the height of the first mesh cell of the surface was set as 8.00×10^{-5} m. The details of the mesh arrangement of the benchmark model, single set-back model, and double set-back model can be found in Figure 4.

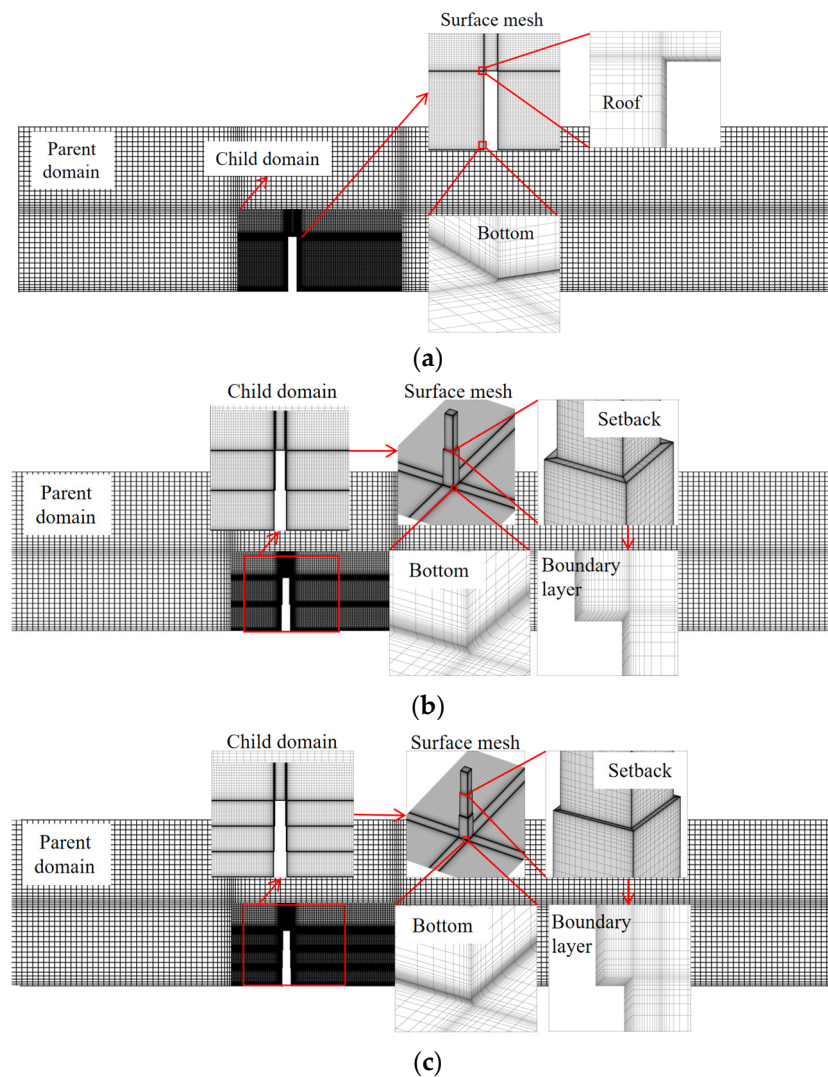


Figure 4. Mesh arrangements of high-rise building models: (a) benchmark; (b) single set-back; (c) double set-back.

Figure 5 displays the distributions of Y^+ values on the surface of the benchmark model, and it can be found that most of the Y^+ values on the surface are below 5, satisfying the requirement for LES [27]. For the set-back building models, the minimum mesh scheme comprised 3.3 million cells within the computational domain.

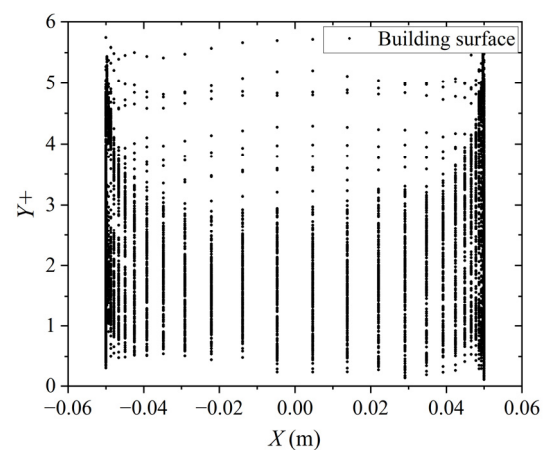


Figure 5. Distribution of Y^+ values on the surface of the benchmark model.

2.3. Boundary Conditions and Solver Settings

The inflow boundary was set as the velocity inlet. According to the logarithmic law, the velocity profile can be defined as [28]

$$U(z) = \frac{u_*}{K} \ln\left(\frac{z+z_0}{z_0}\right) \quad (1)$$

where $u_* = 0.577$ m/s is the frictional velocity, $K = 0.42$ is the Von Karman constant, and $z_0 = 2.25 \times 10^{-4}$ m is roughness length.

The turbulence intensity I_U can be determined by

$$I_U(z) = \begin{cases} 0.05665 - 0.04316 \ln(z+z_0), & z \geq 0.035 \\ 5.71(z+z_0), & z \leq 0.035 \end{cases} \quad (2)$$

The turbulence energy k and turbulent dissipation rate ε are given by

$$k(z) = \frac{3}{2} [U(z) I_U(z)]^2 \quad (3)$$

$$\varepsilon(z) = C_\mu^{3/4} \frac{k(z)^{3/2}}{K(z+z_0)} \quad (4)$$

where $C_\mu = 0.09$ is the model constant.

The non-slip wall was used to simulate the ground and the surface of the set-back building models and the pressure outlet was applied at the outlet boundary. The symmetry boundary was applied at the top and side walls of the domain. In addition, the empty computational domain was used to validate the self-sustaining property of the atmosphere boundary layer.

Figure 6 presents a comparison of the wind profile from inlet, outlet, and the cross-section at the centre of the model obtained from the empty computational domain, with the results calculated by Equations (1) and (2). The numerical simulation results demonstrate a strong correlation with the theoretical values, which indicates that the atmospheric boundary layer has a good self-sustaining ability. Consequently, the proposed LES model is capable of simulating the wind field around set-back tall buildings.

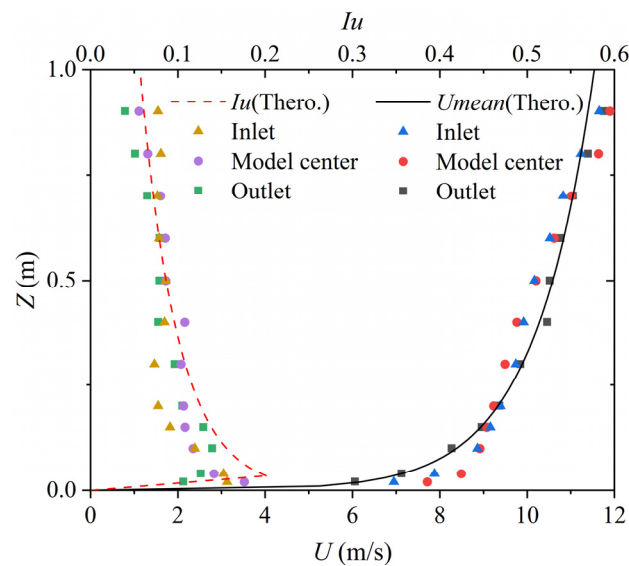


Figure 6. Comparison of the wind profiles obtained from LES, with the result calculated by Equations (1) and (2).

The k-epsilon model was selected to generate the initial flow field for the transient simulation of LES, and the Smagorinsky–Lilly (SM) model was utilized for a LES subgrid

scale model with $C_s = 0.1$. The velocity–pressure coupling was calculated through the SIMPLEC algorithm, all residuals were set to 10^{-5} , and the second-order implicit scheme was taken into account in the solver. To maintain the CFL number below 5, the time step was set as 5×10^{-5} s. The simulation comprises 40,000 steps so that the total duration reaches three Flow Through Domains (FTDs) [29].

2.4. Grid Sensitive Test

After the dimensionless treatment, the wind pressure coefficients $C_{pi,mean}$ and $C_{pi,rms}$ can be obtained from the wind pressure on the surface of the set-back building; that is,

$$C_{pi,mean} = \frac{P_i - P_0}{\frac{1}{2}\rho U_H^2} \quad (5)$$

$$C_{pi,rms} = \frac{\sigma_{pi}}{\frac{1}{2}\rho U_H^2} \quad (6)$$

where P_i is the measured wind pressure at i tap, $P_0 = 0$ Pa is the pressure at the reference height, U_H is the velocity of the incoming wind at the top of the model, and σ_{pi} is the root mean square of the pulsating pressure.

Two additional grid types, with the thickness of the first layer boundary mesh of 5.00×10^{-5} m and 1.00×10^{-4} m, were selected for grid sensitive analysis to verify the resolution of the model. When the mesh sizes did not exceed 8.0×10^{-5} m, the results of numerical simulation were close. To assess the accuracy of the proposed models, the results of benchmark model (case 1) were compared to that of the wind tunnel test performed by Zheng et al. [28]. It can be observed that the mean wind pressure coefficient $C_{pi,mean}$ obtained from the LES exhibits strong concordance with the experimental results (see Figure 7a). The fluctuating wind pressure coefficient $C_{pi,rms}$ obtained from the LES is slightly larger than that from the wind tunnel test (see Figure 7b). Nevertheless, all the curves display a consistent trend, suggesting that the proposed LES models are dependable for evaluating the aerodynamic performance of set-back tall buildings.

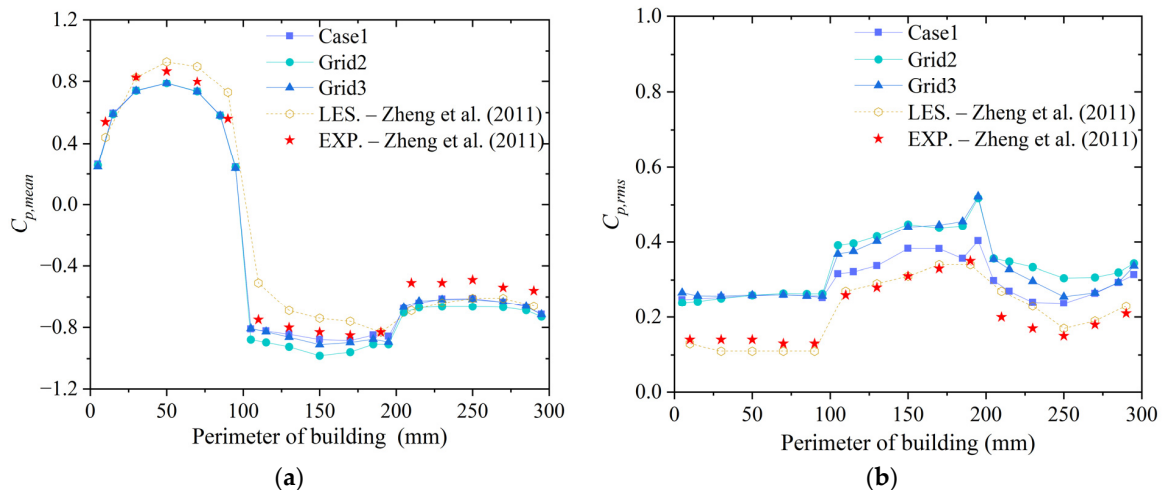


Figure 7. Comparison of wind pressure coefficient distributions with previous study [28]: (a) mean wind pressure coefficient; (b) RMS wind pressure coefficient.

3. Results and Discussion

A thorough evaluation of the relevant flow mechanisms and aerodynamic performance was conducted due to the complexity of the flow structure around set-back tall buildings. The results of the mean wind pressure and local wind force distribution, power spectral densities of base moment, instantaneous vortex structure, time-averaged flow field, and structural response are discussed in the following section.

3.1. Mean Wind Pressure and Local Wind Force Distribution

The influence of set-back measures on the mean wind load was assessed through the distribution of the mean wind pressure coefficient (see Figure 8). Although the frontal vortex was generated on the windward surface and the negative pressure decreased slightly on the leeward surface for the set-back building models, the difference in $C_{pi,mean}$ between the set-back building models and the benchmark model on these two sides was not significant, as shown in Figure 8a,c.

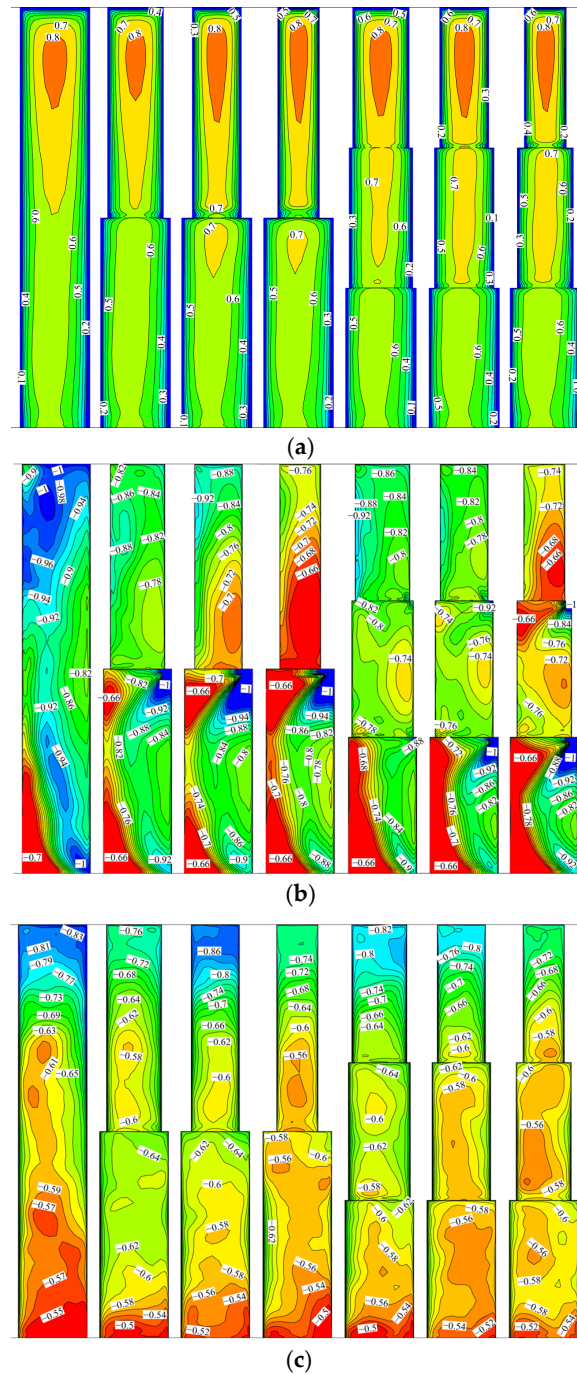


Figure 8. Contour of mean wind pressure coefficients on the surface for the proposed building models: (a) windward; (b) sideward; (c) leeward.

The contour representing the mean wind pressure coefficient on the sideward is displayed in Figure 8b. It can be found that $C_{pi,mean}$ was negative on the sideward surface

due to the effect of flow separation, and the maximum value appeared at the leading edge. Compared to the benchmark model, the zone of peak negative pressure coefficient in the set-back buildings remarkably decreased. For Group 1, $C_{pi,mean}$ at the trailing edge exhibited a rebound near the steps and ground due to the reattachment of the separated flow, resulting in a further reduction in the fluctuating cross-wind pressure.

According to the wind pressure distribution on the building surface, the dimensionless local wind coefficients $C_{D,mean}(z_i)$, $C_{D,rms}(z_i)$, and $C_{L,rms}(z_i)$ were used to further evaluate the actual aerodynamic optimization effects of the set-back measures; that is,

$$C_{D,mean}(z_i) = \frac{F_{D,mean}(z_i)}{\frac{1}{2}\rho U_H^2 A(z_i)} \quad (7)$$

$$C_{D,rms}(z_i) = \frac{\sigma_{FD}(z_i)}{\frac{1}{2}\rho U_H^2 A(z_i)} \quad (8)$$

$$C_{L,rms}(z_i) = \frac{\sigma_{FL}(z_i)}{\frac{1}{2}\rho U_H^2 A(z_i)} \quad (9)$$

where $F_{D,mean}(z_i)$ is the mean drag force at the measurement layer i ; $\sigma_{FD}(z_i)$ and $\sigma_{FL}(z_i)$ are the root mean square of drag force and lift force at the measurement layer i , respectively. $A(z_i)$ is the frontal area of the measurement layer i .

Figure 9 provides a comparison of the local wind force coefficients for the proposed building models. It can be found from Figure 9a that the effect of set-back measures on the mean drag coefficient was negligible. Meanwhile, the effect of set-back measures on the fluctuating drag coefficient was greatest at $0.7H$ (see Figure 9b). It should be mentioned that the fluctuating lift coefficient dropped significantly with the increase in set-back length, as shown in Figure 9c. Moreover, the actual aerodynamic optimization effect of Group 1 was more stable than that of Group 2.

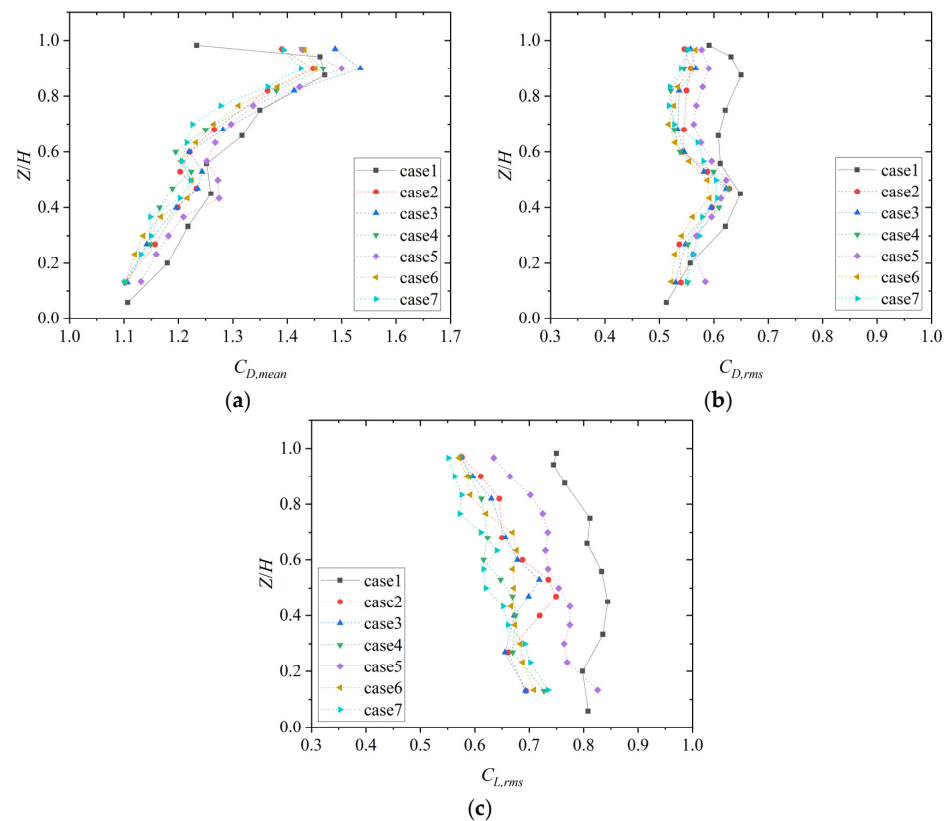


Figure 9. Comparison of the local wind force coefficients for the proposed building models: (a) $C_{D,mean}$; (b) $C_{D,rms}$; (c) $C_{L,rms}$.

3.2. Power Spectral Densities of Base Moment

The time history of the dimensionless base moment coefficients was used to reflect the integral transient wind effects of building, which can be defined as

$$C_{Mx} = \frac{Mx}{\frac{1}{2}\rho U_H^2 DH^2} \quad (10)$$

$$C_{My} = \frac{My}{\frac{1}{2}\rho U_H^2 DH^2} \quad (11)$$

$$C_{Mz} = \frac{Mz}{\frac{1}{2}\rho U_H^2 BDH} \quad (12)$$

where C_{Mx} , C_{My} , and C_{Mz} are the mean base moment coefficients of the along-wind, cross-wind, and torsional directions. Mx , My , and Mz are the corresponding base moments obtained from the LES.

The time history of the base moment coefficients can be converted into power spectral densities (PSDs) by using Fourier transform; thus, the variation in the wind effects of the proposed building models in the frequency domain can be examined. Figure 10 illustrates a comparison of the PSDs of base moment for the proposed building models in the along-wind, cross-wind, and torsional directions, in which the ordinate denotes the power spectral densities and the abscissa denotes the reduced frequency. It can be found in Figure 10a that the spectrum exhibited broadband characteristics without obvious peaks for all building models in the along-wind direction. Figure 10b shows that the PSDs diminished with the increase in the length of set-back for both of the two groups of set-back building models, with the maximum peak of the spectrum at 0.128 occurring in case 1 and the minimum peak at 0.009 occurring in case 7. The spectrum of the set-back building models developed from narrowband to broadband, while the spectrum of the benchmark model maintained narrowband characteristics in the cross-wind direction. This indicates that the periodic vortex shedding of set-back buildings was suppressed, leading to a more irregular vortex shedding process. In addition, with the increase in the set-back length, the reduced frequency of the peak spectral energy became higher and the vortex shedding frequency increased. It can be observed in Figure 10c that the spectral energy of the building models was not affected by set-back measures in the torsional direction, indicating that the spectral energy of the building models in the torsional direction was negligible compared to that in the along-wind and cross-wind directions.

3.3. Instantaneous Vortex Structure

The Q-criterion is regarded as a general approach to visually analysing the vortex structure in a flow field, and it can be defined as follows:

$$s_{ij} = \frac{1}{2} \left(\frac{\partial u_i}{\partial x_j} + \frac{\partial u_j}{\partial x_i} \right), r_{ij} = \frac{1}{2} \left(\frac{\partial u_i}{\partial x_j} - \frac{\partial u_j}{\partial x_i} \right) \quad (13)$$

where s_{ij} and r_{ij} are the strain rate and the rotation rate, respectively.

In order to accurately capture the representative vortex structures in different set-backs, the value of Q was set to 3000 in this study. Figure 11 displays typical diagrams of three-dimensional transient vortex structures around the proposed building models. The flow field of the set-back building models was similar to that of the benchmark model, which was characterized by the generation of z horseshoe vortex on the ground, z separated vortex at the roof, and an elevated vortex on the sideward surface. It is noteworthy that the set-back measures disrupted the coherence of the vortex structures, resulting in more fragmentary vortex structures around the set-back building models. Furthermore, the coherence of the vortex structure in Group 1 was less obvious than that in Group 2. This is primarily attributed to the abrupt change in the cross-section of the single set-back

buildings. When compared to the benchmark building, the extension of the wake vortex around the set-back buildings was shorter. The wake region of the set-back building models could not generate strong vortex shedding.

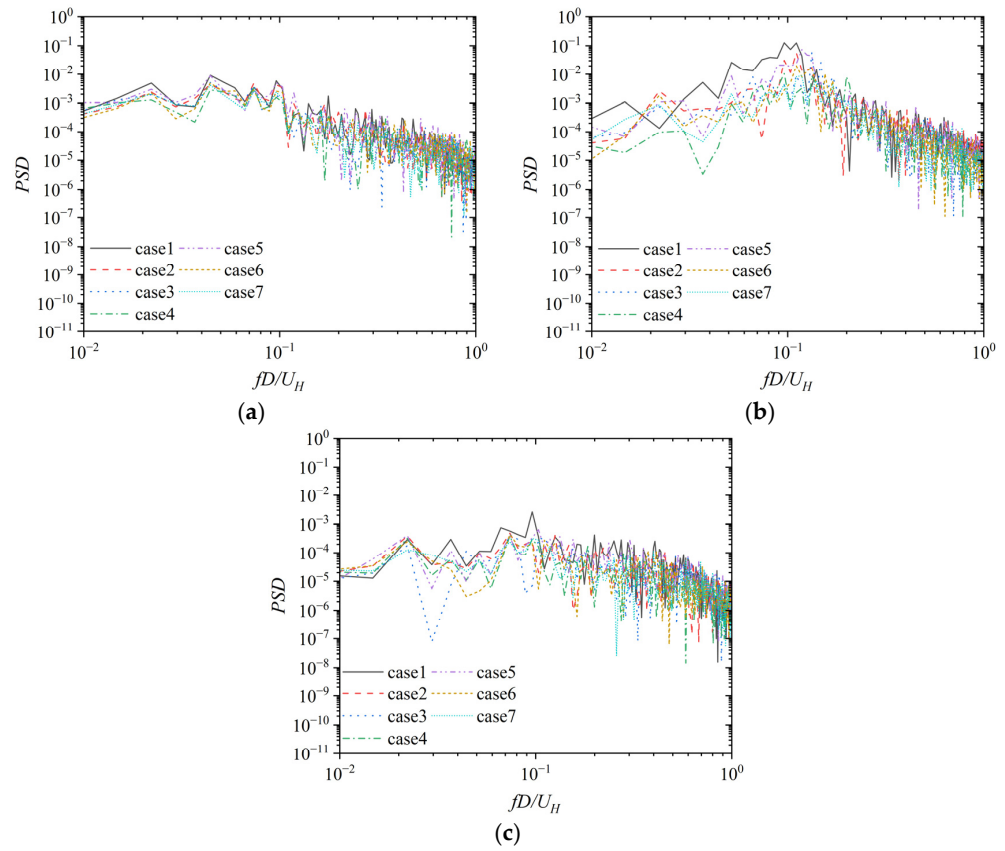


Figure 10. Comparison of PSDs of base moment of the proposed building models: (a) along-wind direction; (b) cross-wind direction; (c) torsional direction.

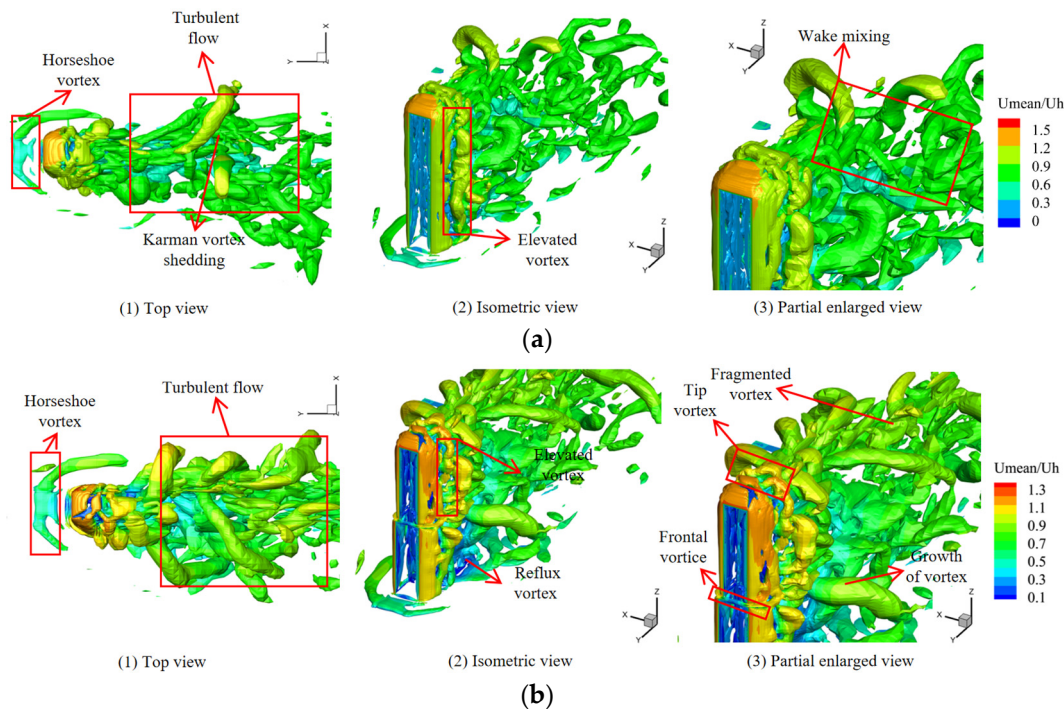


Figure 11. Cont.

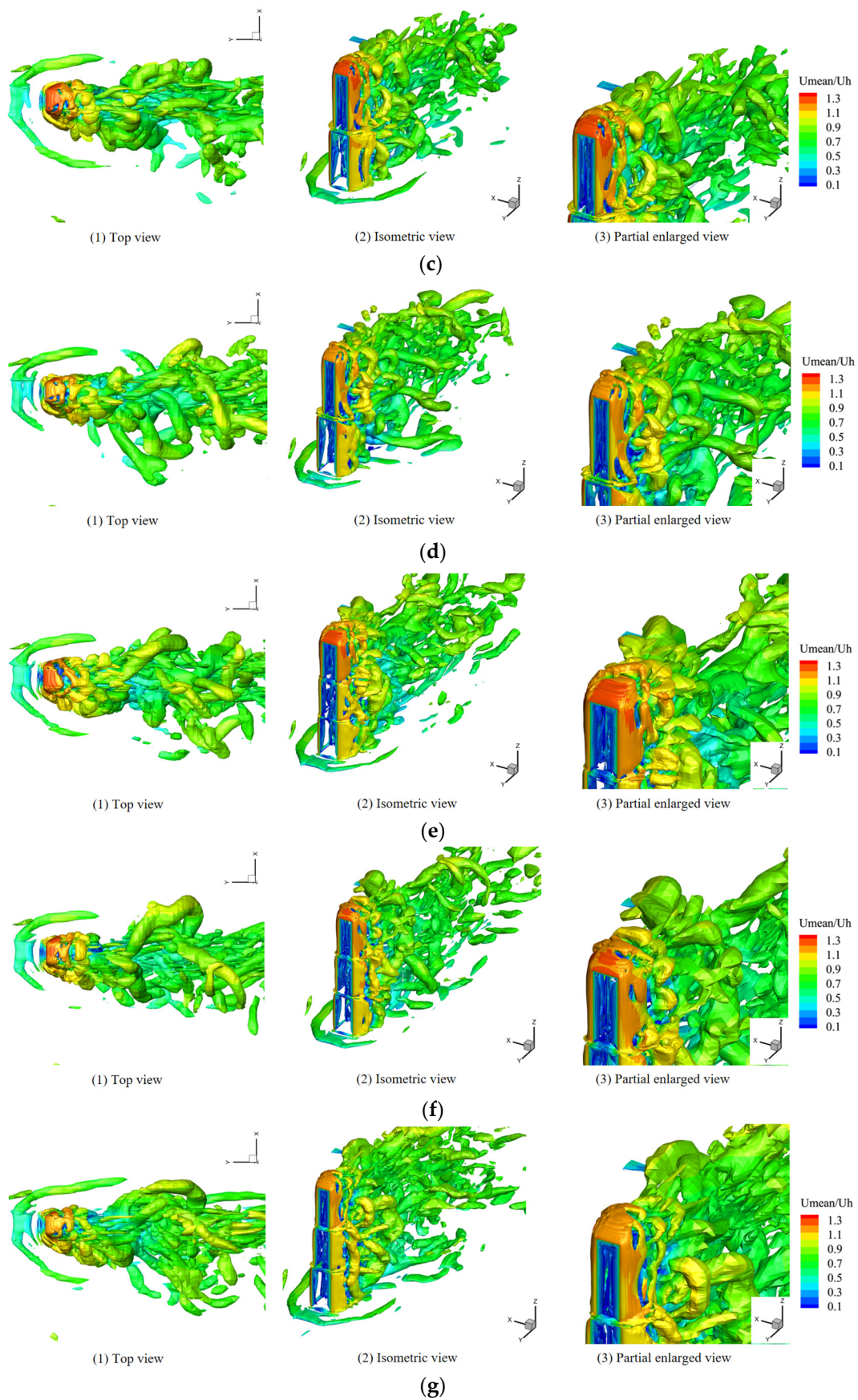
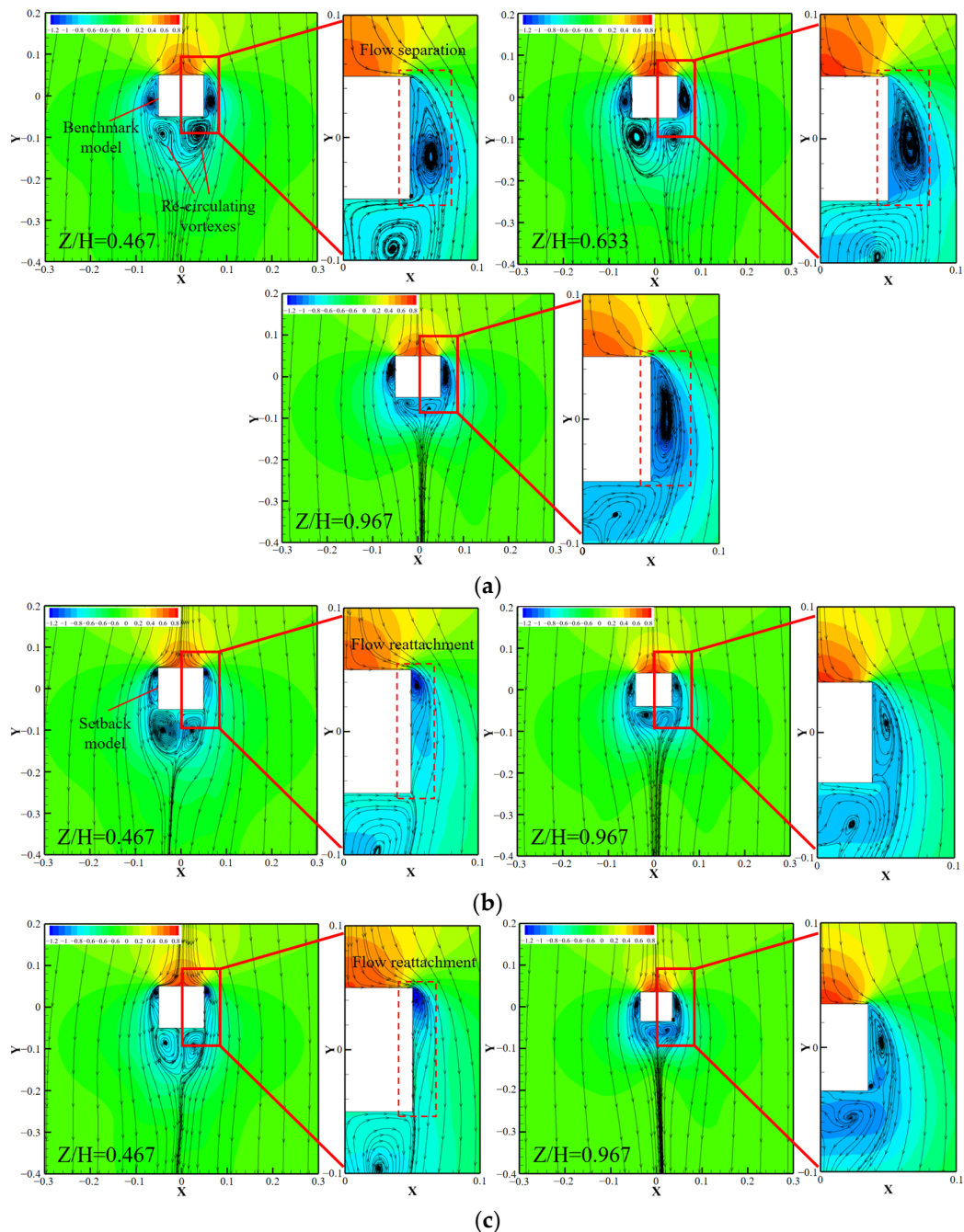


Figure 11. Typical diagrams of three-dimensional transient vortex structures around the proposed building models: (a) case 1; (b) case 2; (c) case 3; (d) case 4; (e) case 5; (f) case 6; (g) case 7.

3.4. Time-Averaged Flow Field

In order to obtain the time-averaged flow field of the representative plane, the X–Y horizontal planes at $Z/H = 0.467, 0.633,$ and 0.967 were extracted from the benchmark model. Similarly, the X–Y horizontal planes at $Z/H = 0.467$ and 0.967 were obtained from Group 1, and the X–Y horizontal planes at $Z/H = 0.633$ and 0.967 were derived from Group 2. Figure 11 shows the streamline diagram of the mean velocity of the proposed building models at different horizontal planes. It can be observed that the inflow reached the windward surface first and spread to both sides, and then the flow separated at the leading edge of the sideward surface. Finally, a pair of symmetrical swirling vortices were generated in the wake region of the model on the leeward. The streamline at the height of $Z/H = 0.967$ for the building models adhered to the leeward surface due to the influence of the three-dimensional vortex.



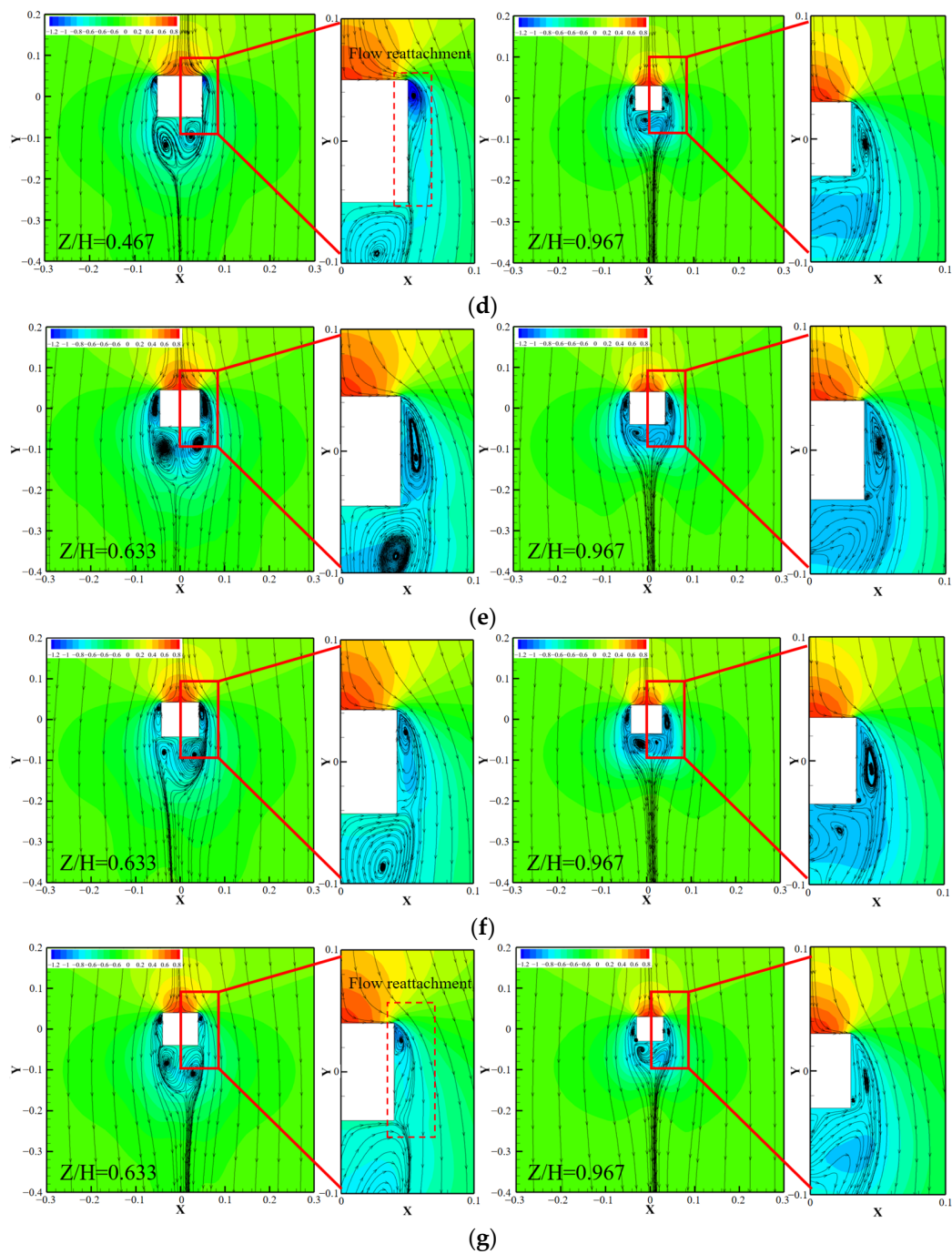


Figure 11. Streamline diagram of mean velocity of the building models at different horizontal planes: (a) case 1; (b) case 2; (c) case 3; (d) case 4; (e) case 5; (f) case 6; (g) case 7.

It can be observed in Figure 11a,d,g that the set-back measures could decrease the width of the wake region on the leeward by reducing the contact area. Furthermore, the aerodynamic performance in the cross-wind direction improved due to the decrease in the separation vortex sizes in the sideward surface of the set-back building models (see Figure 11a,b,e). It can also be observed from Figure 11b–d that the reattachment of the separated shear layers occurred sideward of the single set-back building models (Group 1), and the flow reattachment reduced the turbulence intensity and aerodynamic force in the cross-wind direction.

3.5. Structural Response

To take account of the amplification effect, the base peak dynamic moment $M_{D,max}$ was used to describe the comprehensive structural response of full-scale building in this study, which can be defined as

$$M_{D,max} = M_{mean} + g\sigma_{MD} \quad (14)$$

where M_{mean} is the mean value of the base dynamic moment M ; $g = 3\sim 4$ denotes the peak factor; and σ_{MD} is the root mean square of the base dynamic moment, which can be calculated by

$$\sigma_{MD} = \sqrt{\int_0^{\infty} |H(f)|^2 S_M(f) df} \approx \sqrt{\sigma_{M,B}^2 + \sigma_{M,R}^2} \quad (15)$$

where $S_M(f)$ is the PSD of the base peak dynamic moment, and $|H(f)|^2$ is the mechanical admittance function. $\sigma_{M,B}$ and $\sigma_{M,R}$ are the background and resonant response of building, respectively.

In order to obtain $M_{D,max}$, the first-order and second-order inherent frequencies were set as 0.16 Hz, and the structural damping (ζ_0) was chosen as 3.5%. The base peak dynamic moments of the proposed building models (case 1–case 7) in both the along-wind and cross-wind directions can be found in Figures 12a and 12b, respectively.

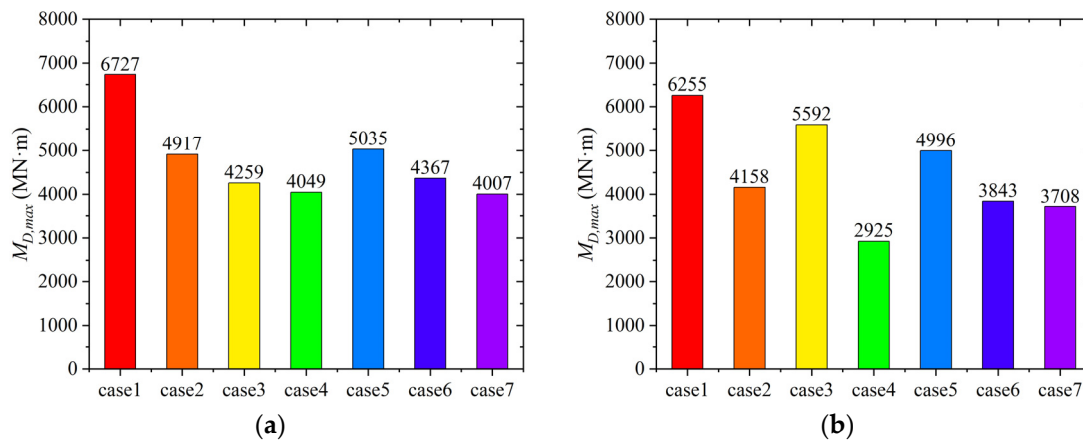


Figure 12. Comparison of base peak dynamic moment of different set-back building models: (a) along-wind direction; (b) cross-wind direction.

For the along-wind direction, the base peak dynamic moment decreased slowly with the increase in the set-back length in each group. In addition, the effect of step numbers on the base peak dynamic moment was limited. The maximum reduction in the base peak dynamic moment of the set-back building reached 40.4% compared to the benchmark model.

For the cross-wind direction, the base peak dynamic moment decreased rapidly with the increase in the set-back length in each group except case 3. Furthermore, the aerodynamic performance of the single set-back buildings was superior to that of double set-back buildings. The aerodynamic performance of case 4, which has the longest distance between the edges of set-back and base, proved to be the most outstanding one. It should be noted that $M_{D,max}$ rebounded to 5592 MN·m, which was 31.3% higher than that in the along-wind direction for case 3 due to the vortex-induced vibration (VIV). Specifically, the unusual phenomenon in case 3 was primarily ascribed to the growth in the resonant response.

Figure 13 further analyses the impact of VIV on the structural response in the cross-wind direction, in which the top peak acceleration response a_{\max} of the set-back tall buildings can be obtained from Equation (16):

$$a_{\max} = \frac{g}{k_p H} \sqrt{\int_0^{\infty} (2\pi f)^4 |H(f)|^2 S_M(f) df} \quad (16)$$

where k_p is the modal stiffness.

It can be found from Figure 13 that the top peak acceleration response of case 3 was 30% larger than that of the benchmark model in the cross-wind direction due to VIV, which might severely impact human comfort. Meanwhile, the effects of the set-back measures on the top peak acceleration response of the other cases (case 2, 4, 5, 6, 7) in the cross-wind direction were limited.

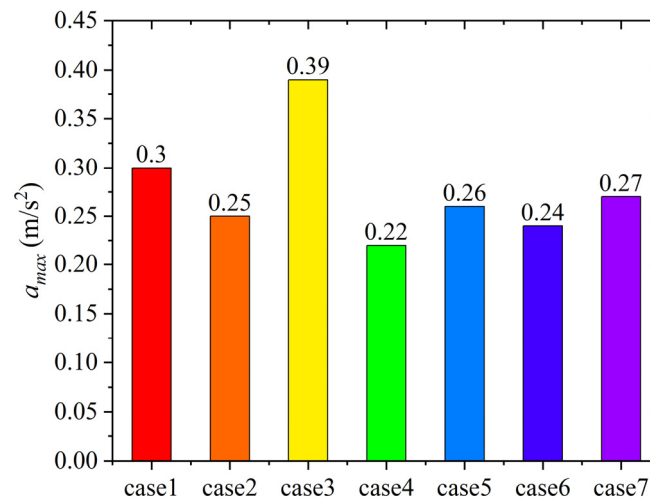


Figure 13. Comparison of the top peak acceleration of different set-back building models in the cross-wind direction.

VIV exerts a detrimental effect on the structural responses of high-rise buildings in the cross-wind direction. However, the effect of cross wind was always ignored by wind engineers. In this study, the PSDs of modal-weighted aerodynamic force F_m were studied to understand the influence of cross-wind aerodynamic forces on the structural response of set-back tall buildings. F_m can be calculated as follows:

$$F_m = \varphi F(z, t) \quad (17)$$

$$\varphi = z/H \quad (18)$$

where $F(z, t)$ is the time-history of the wind force and φ is the first-order modal of the building.

Figure 14 illustrates the distribution of PSDs of F_m and $S_{F_m}(f)$ along the height of the proposed building models in the cross-wind direction. The peak spectral energy for Group 1 was observed at 0.82 H, 0.82 H, and 0.40 H, while for Group 2, it appeared at 0.83 H, 0.50 H, and 0.43 H, respectively. This indicates that the dominant aerodynamic forces occurred at the middle-upper part of the set-back building models. Hence, additional local aerodynamic optimization needs to be adopted in the corresponding positions to avoid VIV. Furthermore, according to Figure 14d,g, increasing the length of set-back could reduce the probability of the occurrence of VIV. This is attributed to the vortex shedding frequency of the wake becoming disordered when the energy spectrum was divided into two parts.

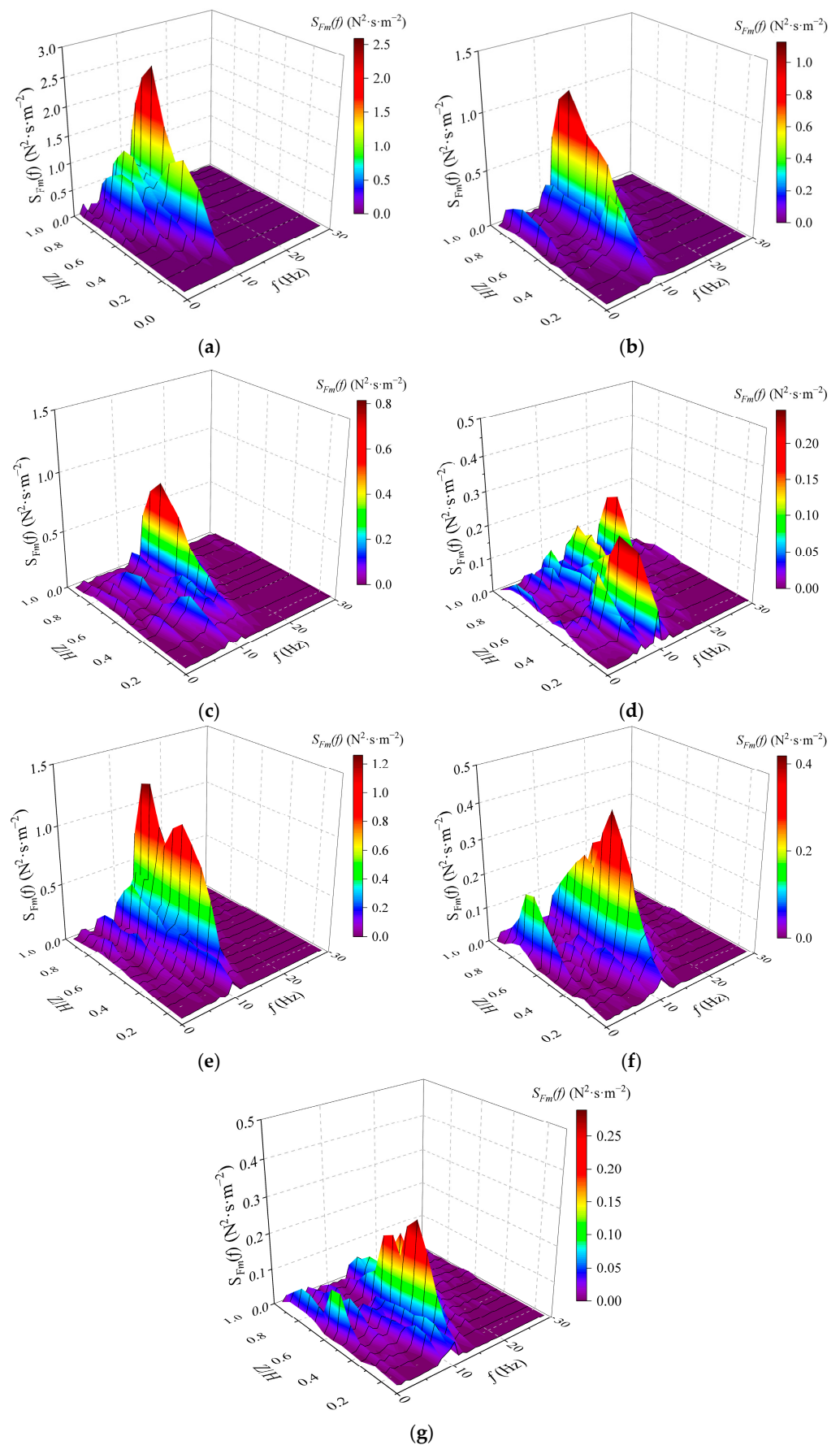


Figure 14. Distribution of PSDs of modal-weighted aerodynamic force along height in the cross-wind direction: (a) case 1; (b) case 2; (c) case 3; (d) case 4; (e) case 5; (f) case 6; (g) case 7.

4. Conclusions

In this paper, the flow mechanism and aerodynamic performance of set-back tall buildings were investigated through LES technique. The results of the mean wind pressure and local wind force distribution, power spectral densities of base moment coefficients, flow field distribution, and structural responses of set-back building models were discussed. The main conclusions can be drawn as follows:

- (1) The set-back measures can reduce the mean wind pressure coefficients on the surface of high-rise buildings, especially for the sideward surface. The set-back measures have an actual optimization effect on the $C_{D,rms}$ and $C_{L,rms}$, while the effect on the distribution of $C_{D,mean}$ is limited.
- (2) The set-back measures have a significant impact on the power spectral densities of cross-wind base moment coefficients of a building, and the maximum reduction can reach 93%. As the length of set-back increases, the spectrum of set-back building models develops from narrowband to broadband and the intensity of vortex shedding weakens.
- (3) As the length of set-back increases in each group, more fragmentary vortex structures are generated so that the regular and strong vortex shedding are suppressed. The set-back measures in Group 1 can weaken the coherence of the vortex structure more than that of Group 2.
- (4) The reduction in wake width of the set-back building models mainly comes from the decrease in contact area. The set-back measures motivate the reattachment of separated shear layers on the sideward surface of buildings in Group 1, thus the cross-wind forces decrease.
- (5) As the length of set-back increases, the base peak dynamic moment in the cross-wind direction decreases more significantly than that in the along-wind direction in each group, and the maximum reduction can reach 53.2% in the cross-wind direction while reaching only 40.4% in the along-wind direction. On the whole, the comprehensive aerodynamic performance of single set-back structures is slightly better than that of the double set-back structures. The amplification of structural response in the cross-wind direction caused by VIV can be avoided by additional local aerodynamic optimization at the middle-upper part of the set-back building.

Author Contributions: Conceptualization, W.-H.L. and N.-T.Y.; methodology, W.-H.L.; software, W.-H.L.; validation, W.-H.L. and Y.Z.; formal analysis, W.-H.L. and Y.Z.; investigation, W.-H.L. and N.-T.Y.; resources, W.-H.L. and N.-T.Y.; data curation, W.-H.L. and Y.Z.; writing—original draft preparation, W.-H.L. and N.-T.Y.; writing—review and editing, N.-T.Y.; visualization, Y.Z.; supervision, N.-T.Y.; project administration, W.-B.Y.; funding acquisition, W.-B.Y. All authors have read and agreed to the published version of the manuscript.

Funding: This research was funded by the Research Funding of Zhejiang University of Technology, grant number No. SH1060210983.

Data Availability Statement: The data presented in this study are available on request from the corresponding author.

Conflicts of Interest: Author Nan-Ting Yu was employed by the company Huzhou Green New Material Co., Ltd. The remaining authors declare that the research was conducted in the absence of any commercial or financial relationships that could be construed as a potential conflict of interest.

References

1. El Ouni, M.H.; Abdeddaim, M.; Elias, S.; Kahla, N.B. Review of vibration control strategies of high-rise buildings. *Sensors* **2022**, *22*, 8581. [[CrossRef](#)]
2. Sharma, A.; Mittal, H.; Gairola, A. Mitigation of wind load on tall buildings through aerodynamic modifications. *J. Build. Eng.* **2018**, *18*, 180–194. [[CrossRef](#)]
3. Wijesooriya, K.; Mohotti, D.; Lee, C.K.; Mendis, P. A technical review of computational fluid dynamics (CFD) applications on wind design of tall buildings and structures: Past, present and future. *J. Build. Eng.* **2023**, *74*, 106828. [[CrossRef](#)]

4. Yuan, W.B.; Yu, N.T.; Wang, Z. The effects of grooves on wind characteristics of tall cylinder buildings. *Wind Struct.* **2018**, *26*, 89–98.
5. Ilgin, H.E. Space efficiency in tapered super-tall towers. *Buildings* **2023**, *13*, 2819. [[CrossRef](#)]
6. Sharma, A.; Mittal, H.; Gairola, A. Wind-induced forces and flow field of aerodynamically modified buildings. *Environ. Fluid Mech.* **2019**, *19*, 1599–1623. [[CrossRef](#)]
7. Kim, Y.; Kanda, J. Characteristics of aerodynamic forces and pressures on square plan buildings with height variations. *J. Wind Eng. Ind. Aerodyn.* **2010**, *98*, 449–465. [[CrossRef](#)]
8. Cooper, K.R.; Nakayama, M.; Sasaki, Y.; Fediw, A.A.; Resende-Ide, S.; Zan, S.J. Unsteady aerodynamic force measurements on a super-tall building with a tapered cross section. *J. Wind Eng. Ind. Aerodyn.* **1997**, *72*, 199–212. [[CrossRef](#)]
9. Kim, W.; Yoshida, A.; Tamura, Y.; Yi, J.H. Experimental study of aerodynamic damping of a twisted supertall building. *J. Wind Eng. Ind. Aerodyn.* **2018**, *176*, 1–12. [[CrossRef](#)]
10. Chen, Z.S.; Ning, G.L.; Zhang, L.K.; Xue, X.Y.; Wang, S.Y.; Xu, Y.M.; Yuan, C.F.; Tse, T.K.; Li, C.Y.; Xue, X.Y. A comprehensive study of the aerodynamic characteristics of an aspect ratio of 6.25: 1 inclined square prism. *Front. Physics* **2023**, *11*, 1180778. [[CrossRef](#)]
11. Chen, F.B.; Wang, X.L.; Zhao, Y.; Li, Y.B.; Li, Q.S.; Xiang, P.; Li, Y. Study of wind loads and wind speed amplifications on high-rise building with opening by numerical simulation and wind tunnel test. *Adv. Civ. Eng.* **2020**, *2020*, 8850688. [[CrossRef](#)]
12. Sharma, A.; Mittal, H.; Gairola, A. Aerodynamics of tapered and set-back buildings using detached-eddy simulation. *Wind Struct.* **2019**, *29*, 111–127.
13. Kim, Y.C.; Tamura, Y.; Tanaka, H.; Ohtake, K.; Bandi, E.K.; Yoshida, A. Wind-induced responses of super-tall buildings with various atypical building shapes. *J. Wind Eng. Ind. Aerodyn.* **2014**, *133*, 191–199. [[CrossRef](#)]
14. Tanaka, H.; Tamura, Y.; Ohtake, K.; Nakai, M.; Kim, Y.C. Experimental investigation of aerodynamic forces and wind pressures acting on tall buildings with various unconventional configurations. *J. Wind Eng. Ind. Aerodyn.* **2012**, *107*, 179–191. [[CrossRef](#)]
15. Kim, Y.C.; Kanda, J. Wind pressures on tapered and set-back tall buildings. *J. Fluids Struct.* **2013**, *39*, 306–321. [[CrossRef](#)]
16. Bairagi, A.K.; Dalui, S.K. Estimation of wind load on stepped tall building using CFD simulation. *Iran. J. Sci. Technol.-Trans. Civ. Eng.* **2021**, *45*, 707–727. [[CrossRef](#)]
17. Bairagi, A.K.; Dalui, S.K. Wind environment around the setback building models. *Build. Simul.* **2021**, *14*, 1525–1541. [[CrossRef](#)]
18. Rajasekarababu, K.B.; Vinayagamurthy, G.; Selvi, R.S. Evaluation of CFD URANS turbulence models for the building under environmental wind flow with experimental validation. *J. Appl. Fluid Mech.* **2022**, *15*, 1387–1401.
19. Rajasekarababu, K.B.; Vinayagamurthy, G. Experimental and computational simulation of an open terrain wind flow around a setback building using hybrid turbulence models. *J. Appl. Fluid Mech.* **2019**, *12*, 145–154. [[CrossRef](#)]
20. Blocken, B. LES over RANS in building simulation for outdoor and indoor applications: A foregone conclusion? *Build. Simul.* **2018**, *11*, 821–870. [[CrossRef](#)]
21. Shirzadi, M.; Mirzaei, P.A.; Tominaga, Y. CFD analysis of cross-ventilation flow in a group of generic buildings: Comparison between steady RANS, LES and wind tunnel experiments. *Build. Simul.* **2020**, *13*, 1353–1372. [[CrossRef](#)]
22. Feng, C.; Gu, M. CFD simulation of wind loads of kilometer-scale super tall buildings with typical configurations in veering wind field. *Struct. Des. Tall Spec. Build.* **2024**, *33*, e2066. [[CrossRef](#)]
23. Li, Y.; Zhu, Y.; Chen, F.B.; Li, Q.S. Aerodynamic loads of tapered tall buildings: Insights from wind tunnel test and CFD. *Structures* **2023**, *56*, 104975. [[CrossRef](#)]
24. Xing, J. Simulation of a ground-mounted prism in ABL flow using LES: On overview of error metrics and distribution. *Adv. Aerodynam.* **2023**, *5*, 9. [[CrossRef](#)]
25. Franke, J.; Hellsten, A.; Schlünzen, H.; Carissimo, B. The COST 732 Best Practice Guideline for CFD simulation of flows in the urban environment: A summary. *Int. J. Environ. Pollut.* **2011**, *44*, 419–427. [[CrossRef](#)]
26. Park, S.J.; Kim, J.J. Development of a computational fluid dynamics model adopting a nested grid system: Flow simulations for ideal and real urban settings. *Urban Clim.* **2024**, *53*, 101801. [[CrossRef](#)]
27. Tamura, T.; Nozawa, K.; Kondo, K. AIJ guide for numerical prediction of wind loads on buildings. *J. Wind Eng. Ind. Aerodyn.* **2008**, *96*, 1974–1984. [[CrossRef](#)]
28. Zheng, D.Q.; Gu, M.; Zhang, A.S.; Zhang, J.G. Large eddy simulation of flow around a single square building model with 1:1:6 shape. *J. Vib. Shock* **2011**, *30*, 96–100.
29. Thordal, M.S.; Bennetsen, J.C.; Koss, H.H.H. Review for practical application of CFD for the determination of wind load on high-rise buildings. *J. Wind Eng. Ind. Aerodyn.* **2019**, *186*, 155–168. [[CrossRef](#)]

Disclaimer/Publisher’s Note: The statements, opinions and data contained in all publications are solely those of the individual author(s) and contributor(s) and not of MDPI and/or the editor(s). MDPI and/or the editor(s) disclaim responsibility for any injury to people or property resulting from any ideas, methods, instructions or products referred to in the content.